

New Phase of MnSb_2O_6 Prepared by Ion Exchange: Structural, Magnetic, and Thermodynamic Properties

Vladimir B. Nalbandyan,^{*,†} Elena A. Zvereva,[‡] Alexey Yu. Nikulin,[†] Igor L. Shukaev,[†] Myung-Hwan Whangbo,[§] Hyun-Joo Koo,^{||} Mahmoud Abdel-Hafez,^{⊥,¶} Xiao-Jia Chen,[⊥] Changhyun Koo,[∇] Alexander N. Vasiliev,^{‡,○,◆} and Rüdiger Klingeler^{∇,△}

[†]Chemistry Faculty, Southern Federal University, 7 ul. Zorge, Rostov-na-Donu, 344090 Russia

[‡]Faculty of Physics, Moscow State University, Moscow, 119991 Russia

[§]Department of Chemistry, North Carolina State University, Raleigh, North Carolina 27695-8204, United States

^{||}Department of Chemistry and Research Institute for Basic Science, Kyung Hee University, Seoul 130-701, Republic of Korea

[⊥]Center for High Pressure Science and Technology Advanced Research, 1690 Cailun Road, Shanghai 201203, China

[¶]Faculty of Science, Physics Department, Fayoum University, Fayoum 63514, Egypt

[∇]Kirchhoff Institute for Physics, Heidelberg University, Heidelberg D-69120, Germany

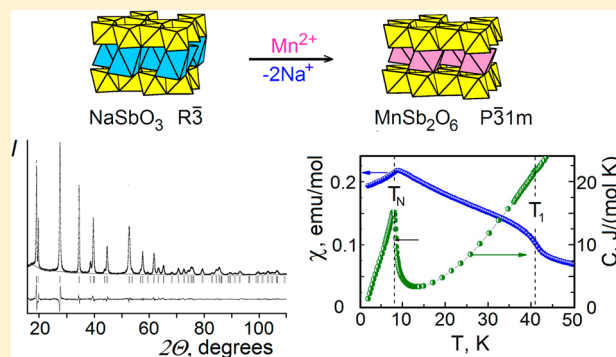
[○]Theoretical Physics and Applied Mathematics Department, Ural Federal University, Ekaterinburg 620002, Russia

[◆]National University of Science and Technology "MISIS", Moscow 119049, Russia

[△]Centre for Advanced Materials, Heidelberg University, Heidelberg 69120, Germany

Supporting Information

ABSTRACT: A new layered trigonal ($P\bar{3}1m$) form of MnSb_2O_6 , isostructural with MSb_2O_6 ($M = \text{Cd}, \text{Ca}, \text{Sr}, \text{Pb}, \text{and Ba}$) and MAs_2O_6 ($M = \text{Mn}, \text{Co}, \text{Ni}, \text{and Pd}$), was prepared by ion-exchange reaction between ilmenite-type NaSbO_3 and $\text{MnSO}_4\text{-KCl-KBr}$ melt at 470 °C. It is characterized by Rietveld analysis of the X-ray diffraction pattern, electron microprobe analysis, magnetic susceptibility, specific heat, and ESR measurements as well as by density functional theory calculations. MnSb_2O_6 is very similar to MnAs_2O_6 in the temperature dependence of their magnetic susceptibility and spin exchange interactions. The magnetic susceptibility and specific heat data show that MnSb_2O_6 undergoes a long-range antiferromagnetic order with Néel temperature $T_N = 8.5(5)$ K. In addition, a weak ferromagnetic component appears below $T_1 = 41.5(5)$ K. DFT+U implies that the main spin exchange interactions are antiferromagnetic, thereby forming spin-frustrated triangles. The long-range ordered magnetic structure of MnSb_2O_6 is predicted to be incommensurate as found for MnAs_2O_6 . On heating, the new phase transforms to the stable $P321$ form via its intermediate disordered variant.



1. INTRODUCTION

Layered oxides of transition metals have attracted much attention since they provide a playground for studying strong electronic correlation effects.^{1–8} In a low-dimensional magnetic sublattice made up of magnetic-ion triangles, geometrical spin frustration arises when the spin exchanges between adjacent magnetic ions are antiferromagnetic (AFM). A large number of fascinating phenomena emerge from such geometrically spin frustrated systems; they include re-entrant phase transitions,^{9,10} magnetization plateaus in the magnetization process,^{11–14} localized magnons in close vicinity of the saturation field,^{11,13,15} magnetic-field-induced spin-Peierls instability,^{16–18} and enhanced magnetocaloric effects.^{19–21} Competing interactions in spin-frustrated systems often result in an unusual

critical behavior near the transitions^{22–24} toward novel phases such as spin ice or quantum spin liquid ground states.^{1,3,25,26} Low-dimensional spin-frustrated systems frequently adopt noncollinear incommensurate spin arrangements to reduce the extent of their spin frustration. Such spin states may remove the inversion symmetry and hence induce finite ferroelectric polarization,^{27,28} as found for the multiferroics TbMnO_3 ,^{29,30} and CoCr_2O_4 ³¹ with cycloidal magnetic structures as well as for the delafossite family AMO_2 ($A = \text{Cu}, \text{Ag}; M = \text{Fe}, \text{Cr}$)^{32–36} with helical magnetic order. Quite recently, MnSb_2O_6 was found to show a chiral crystal structure and corotating cycloidal

Received: November 4, 2014

Published: January 26, 2015

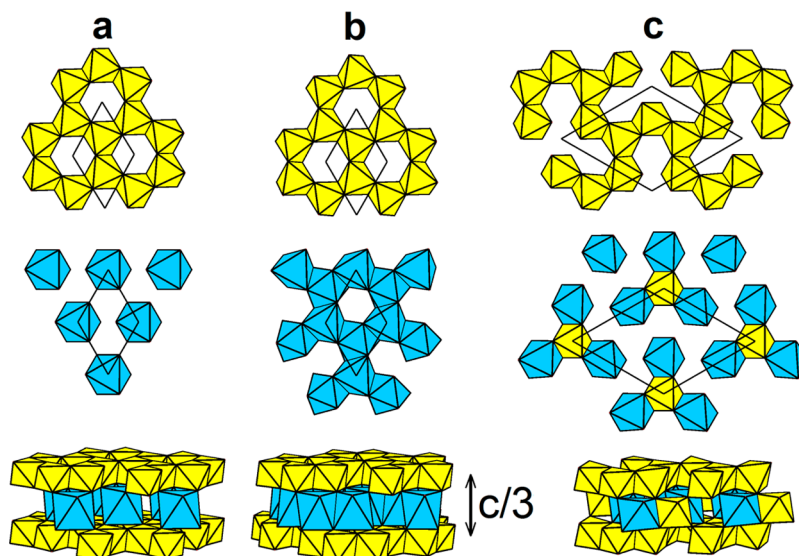


Figure 1. Polyhedral presentation of the crystal structures of (a) CaSb_2O_6 ($P\bar{3}1m$),⁴⁵ (b) NaSbO_3 ($\text{Na}_2\text{Sb}_2\text{O}_6$, $R\bar{3}$),⁴⁶ and (c) MnSb_2O_6 ($P321$).⁴² (Top row) Layer of SbO_6 octahedra, (middle row) MO_6 octahedra ($M = \text{Ca}^{2+}$, Na^+ , or Mn^{2+}), and (bottom row) layer stacking pattern.

magnetic structure, while the presence of concomitant ferroelectric polarization, i.e., multiferroicity, associated with a unique ferroelectric switching mechanism is predicted.³⁷

In the oxides MAS_2O_6 , the magnetic M^{2+} ($M = \text{Mn}$, Co , Ni , and Pd ^{38–40}) and diamagnetic As^{5+} ions are segregated into different layers, but all these arsenates undergo a three-dimensional (3D) AFM ordering at low temperatures. This implies that the interlayer spin exchange interactions are not negligible. Depending on the divalent magnetic cation M^{2+} as well as on the magnetic dipole–dipole interactions, a variety of different magnetic structures is realized in MnAs_2O_6 .⁴¹ Examples are an incommensurate magnetic structure in MnAs_2O_6 , an unusual ferromagnetic contribution to the magnetic susceptibility in NiAs_2O_6 ³⁸ and an anomalously high Néel temperature in PdAs_2O_6 .^{39,40}

Previously, the corresponding antimonates MSb_2O_6 of the same structure type have been only known with nonmagnetic M^{2+} . However, a detailed investigation of the structure suggests that isostructural phases with magnetic M^{2+} might be feasible. To be specific, there is an intriguing similarity between the three trigonal structure types shown in Figure 1: MnSb_2O_6 (space group $P321$),^{37,42} MSb_2O_6 ($M = \text{Pb}$,⁴³ Cd ,⁴⁴ Ca , Sr , and Ba ,⁴⁵ space group $P\bar{3}1m$), and NaSbO_3 ⁴⁶ (or $\text{Na}_2\text{Sb}_2\text{O}_6$, ilmenite type, space group $R\bar{3}$). All of them are based on a double-layered hcp array of oxygen anions with cations occupying octahedral voids. The structures differ in the filling modes of these voids. The PbSb_2O_6 type (Figure 1a) has one formula unit (two oxygen layers) in a hexagonal unit cell, such that Sb occupies 2/3 voids within one layer, thus forming a honeycomb arrangement, while Pb occupies 1/3 voids in the second layer that have no common faces with the SbO_6 octahedra. In NaSbO_3 (Figure 1b), the $\text{SbO}_{6/2}$ layers are essentially the same, but the number of the low-valence cations is doubled, and face-sharing cannot be avoided. Each NaO_6 octahedron shares one face with a SbO_6 octahedron. To avoid sharing both opposite faces, the stacking of the honeycomb layers is hence changed, resulting in a rhombohedral lattice with six oxygen layers (six NaSbO_3 formula units) in the hexagonal cell. The structure of MnSb_2O_6 (Figure 1c) is again double layered. The hexagonal unit cell contains five Sb atoms in one

layer but one Sb and three Mn atoms in the second layer. As a result, the hexagonal axis a is approximately $\sqrt{3}$ times longer than those of PbSb_2O_6 and NaSbO_3 .

The above comparison suggests that several new phases with PbSb_2O_6 -type structure might be obtained by low-temperature ion exchange of NaSbO_3 with suitable salts. Indeed, a new series of layered MSb_2O_6 phases with magnetic M^{2+} cations has been successfully prepared by our group. In the present work we report the preparation and structural, magnetic, and thermodynamic characterization of the first member of the MSb_2O_6 series with PbSb_2O_6 -type structure, a new form of MnSb_2O_6 .

2. EXPERIMENTAL SECTION

2.1. Sample Preparation and Elemental Analysis. All materials used were of reagent grade. Starting NaSbO_3 was prepared by heating a stoichiometric mixture of $\text{Sb}_2\text{O}_3 + 0.6\text{Na}_2\text{CO}_3 + 0.8\text{NaNO}_3$ as reported earlier⁴⁷ and then finely ground with an agate mortar and pestle. Its phase purity was confirmed by powder X-ray diffraction. For the ion-exchange reaction, a low-melting equimolar mixture of MnSO_4 , KCl , and KBr was used with $\text{Mn}:\text{Na}$ ratio of ca. 2.5 (i.e., 5-fold excess against the theoretical quantity). The reaction was performed under CO_2 atmosphere (to prevent oxidation of Mn^{2+}) at 470 °C for 1 h. Considerably higher temperatures or longer heating resulted in an admixture of the known (stable) MnSb_2O_6 form. The cooled product was washed thoroughly with distilled water and dried at room temperature. It is almost white, light grayish-pink, which is a typical color of high-spin Mn^{2+} oxide compounds.

For comparison, the stable MnSb_2O_6 phase was prepared by heating a stoichiometric mixture of Mn_2O_3 and Sb_2O_3 at 600, 900, and 1100 °C for 3 h each with intermittent regrinding and pressing.

Chemical composition of MnSb_2O_6 powders was determined using an electron microprobe apparatus INCA ENERGY 450/XT equipped with an X-Act ADD detector (OXFORD Instruments Analytical) based on an electron microscope VEGA II LMU (Tescan) and operated at 20 kV accelerating voltage. Although the absolute content of each element showed considerable scatter from point to point, their ratios (Mn/Sb and Na/Sb) were much more reproducible. They were averaged over several points in each sample. The results are listed in Table S1, Supporting Information, for two nominally identical samples from separate preparations. They show that the Mn/Sb ratio is essentially stoichiometric, potassium is practically absent, but a small amount of sodium does appear. Its position is discussed in section 3.1.

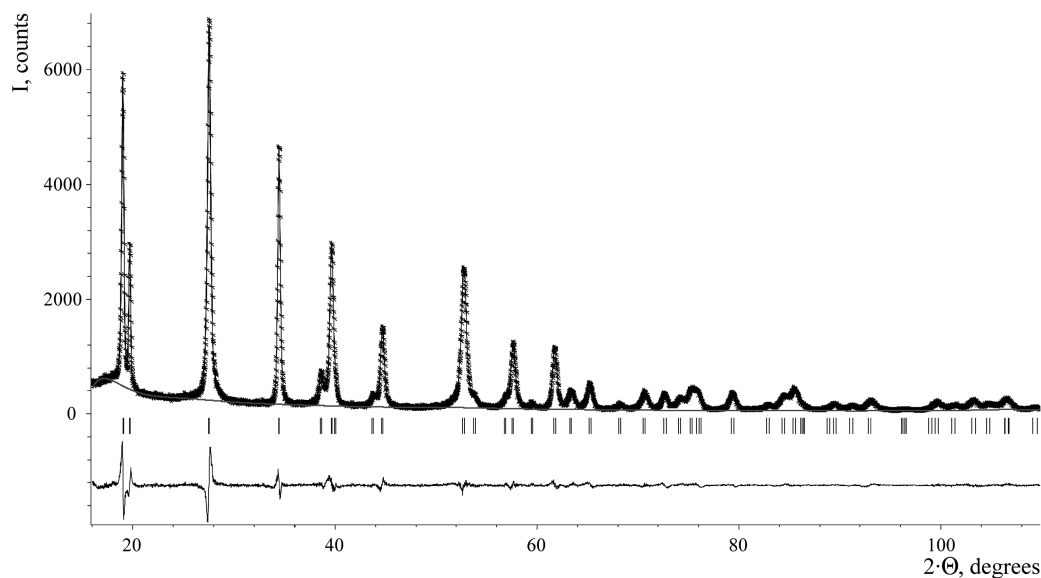


Figure 2. XRD pattern of MnSb_2O_6 , where the points are the experimental data, the line the calculated pattern, the line at the bottom the difference profile, and the vertical bars the peak positions.

Attempts to eliminate the sodium impurity by repeated ion-exchange treatment resulted in partial conversion to the stable form.

2.2. X-ray Diffraction, Magnetic, and Thermophysical Measurements. X-ray diffraction (XRD) was performed using $\text{Cu K}\alpha$ radiation by means of an ARL X'TRA diffractometer equipped with a solid state $\text{Si}(\text{Li})$ detector. To reduce the grain orientation effect, amorphous coffee powder was admixed to the sample. For Rietveld refinements, the GSAS+EXPGUI suite^{48,49} was used. DTA/TGA was done with a STA 449 C/4/G Jupiter instrument (NETZSCH) in air atmosphere.

The static magnetic susceptibility was measured by means of a Quantum Design SQUID XL-5 magnetometer at $B = 0.01$ and 0.1 T in the temperature range $2\text{--}300$ K both after cooling in zero magnetic field (ZFC) and with applied field (FC). Electron spin resonance (ESR) studies were carried out at room temperature using an X-band ESR spectrometer CMS 8400 (ADANI) ($f \approx 9.4$ GHz, $B \leq 0.7$ T). The effective g factor has been calculated with respect to a BDPA (*o*,*g*-bisdiphenyl-*b*-phenylallyl) reference sample with $g_{\text{ref}} = 2.00359$.

Specific heat measurements were carried out by a relaxation method using a Quantum Design PPMS system. A plate-shaped sample of MnSb_2O_6 of ~ 0.25 mm thickness and 6.45 mg mass was used, which had been obtained by cold pressing of the polycrystalline powder. Data were collected at zero magnetic field in the temperature range $2\text{--}300$ K.

3. RESULTS AND DISCUSSION

3.1. Crystal Structure of MnSb_2O_6 . The XRD pattern of the ion-exchange product (Figure 2) is more diffuse than that of the starting NaSbO_3 . This is due most probably to stacking faults created by layer gliding during the ion-exchange transformation between the structures of Figure 1a and 1b. Nevertheless, the pattern was unambiguously indexed by analogy with PbSb_2O_6 -type compounds on a small hexagonal unit cell. No reflections from the starting NaSbO_3 or other impurity phases could be detected. The cubic root of the formula volume of the new phase, together with those for five previously known antimonates, is in reasonable linear relationship with the ionic radii of the divalent cations (Figure 3), thus confirming the adopted composition and structural analogy.

According to the analytical data (Table S1, Supporting Information), the Mn/Sb ratio is essentially stoichiometric (or even slightly overstoichiometric within experimental accuracy),

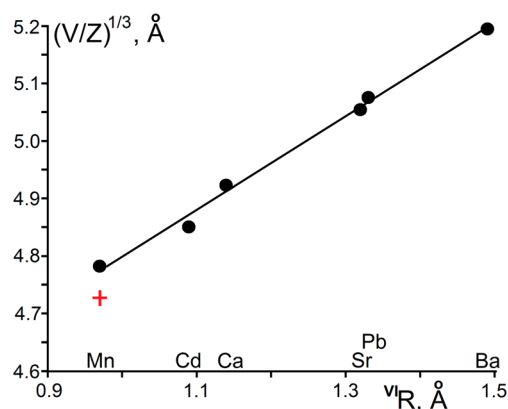
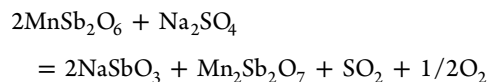


Figure 3. Correlation between the cubic roots of the formula volumes of MSb_2O_6 and the octahedral radii of M^{2+} cations:⁵⁰ (filled circles) PbSb_2O_6 -type phases and (cross) stable MnSb_2O_6 phase.

indicating completion of the ion exchange. Nevertheless, some sodium content was found simultaneously, with a Na/Sb molar ratio of $0.04\text{--}0.05$. Since an electron microprobe only analyzes the thin surface layer, this sodium content might be from adsorbed salts. However, XRD study after calcination at 1100 °C definitely showed besides strong reflections from the stable MnSb_2O_6 weak reflections from NaSbO_3 (see Figure S1 and Table S2, Supporting Information). Using relative intensity ratios (RIR , I/I_{cor}) from the Powder Diffraction File, the weight ratio $\text{NaSbO}_3/\text{MnSb}_2\text{O}_6$ was estimated to be 0.023 , resulting in molar ratio Na/Sb of 0.023 . Another (but nominally identical) sample showed after calcinations a small amount of the third phase, $\text{Mn}_2\text{Sb}_2\text{O}_7$. This may be explained by reactions with adsorbed salts, e.g.



To elucidate the possible presence of sodium in MnSb_2O_6 crystals, five structural models were refined by the Rietveld method: (A) stoichiometric MnSb_2O_6 with no Na impurity; (B) Na substitution on Mn sites, $\text{Mn}^{2+}_{1-2x}\text{Mn}^{3+}_x\text{Na}_x\text{Sb}_2\text{O}_6$; (C)

Na1 substitution on Mn sites compensated by an equivalent amount of Na2 inserted into free octahedra of the Sb layer, $\text{Mn}^{2+}_{1-x}\text{Na}_x\text{Sb}_2\text{O}_6$; (D) same general formula but with Na2 inserted into the Mn layer; (E) the same general formula but with all Na in the Sb layer and x Mn vacancies. Of these, model D is proven unrealistic, whereas models A, B, C, and E provide reasonable agreement factors and thermal parameters with very small differences in R values (for details, see Table S3, Supporting Information). The refined Na content of model C, $x = 0.025(5)$, is close to that found from RIR. However, the corresponding Mn/Sb ratio disagrees with the analytical data, and the interstitial Na2 site in both models C and E seems unrealistic having abnormally short Na–O distances of 2.15 Å, sharing faces with two MnO_6 octahedra and sharing edges with six SbO_6 octahedra. Model B is more reasonable from the crystal-chemistry point of view. However, its refined x value of 0.016(7) (i.e., Na/Sb = 0.08) is close to the experimental uncertainty and cannot explain the analytical data. In addition, the presence of Mn^{3+} disagrees with the magnetic data (see section 3.3) and with the absence of dark coloration typical of mixed-valence Mn compounds. We, therefore, conclude that MnSb_2O_6 under study is essentially sodium free within experimental uncertainties (model A). The sodium impurity may be present as adsorbed salts and, probably, in small nonexchanged ilmenite-type fragments which present as stacking faults in the main phase in accordance with broadened Bragg reflections.

The corresponding crystallographic information file (cif) is given in the Supporting Information. Figure 2 compares the experimental and calculated powder diffraction profiles. Table 1 lists unit cell data, refinement details, and the principal interatomic distances.

Table 1. Crystallographic Data, Refinement Details, and Bond Lengths of MnSb_2O_6 and NaSbO_3

	MnSb_2O_6		NaSbO_3^{46}
	new form	known form ⁴²	
cryst syst	trigonal	trigonal	trigonal
space group	$P\bar{3}1m$ (no. 162)	$P321$ (no. 150)	$R\bar{3}$ (no. 148)
a , Å	5.20649(9)	$8.8011(3) = 5.0813 \times \sqrt{3}$	5.2901(3)
c , Å	4.66276(15)	4.7241(1)	$15.926(2) = 5.309 \times 3$
V , Å ³	109.462(5)	316.90(2)	385.98(6)
Z	1	3	6
fw	394.43	394.43	
density (calcd)	5.984	6.200	
wavelength, Å	1.54056, 1.54439		
angular range (2θ)	16–110°		
no. of data points	4700		
no. of hkl	122		
no. of variables	47		
$R(F^2)$	0.0195		
R_p	0.0761		
R_{wp}	0.0968		
χ^2	3.191		
Mn–O, Å	$2.237(5) \times 6$	2.201 (average)	
Sb–O, Å	$1.998(3) \times 6$	1.984 (average)	1.993 (average)

As can be seen from Figure 1a and 1c the main difference of the new MnSb_2O_6 form from the known one lies in the Sb positions, which move by $c/2$ from the Mn layer to the empty octahedra of the Sb layer. This leads to 2.5% expansion in the a direction (due to the increasing number of short Sb^{5+} – Sb^{5+} distances within the layer) and 1.3% contraction in the c direction, resulting in a volume expansion of 3.6% (see Table 1 and Figure 3). In accordance with this, the Mn–O and Sb–O bond lengths (Table 1) are slightly longer than those in the known form and the corresponding ionic radii sums, 2.19 and 1.96 Å, respectively.⁵⁰ Note that these differences cannot be attributed to the Na impurity: Figure 3 definitely shows that PbSb_2O_6 type (filled circles) is less dense than MnSb_2O_6 type (cross) even if we exclude the point of the new phase.

The new form also differs from the known one by much more regular MnO_6 and SbO_6 octahedra. The O–Mn–O and O–Sb–O bond angles vary in the range of 88.0–92.0° and 82.4–93.3°, respectively, whereas in the known form these ranges are 74.0–98.0° and 79.2–98.2°, respectively.

3.2. Thermal Behavior. Since the ion-exchange product would be a metastable one it is expected to transform irreversibly and exothermally to the known stable form. However, the DTA scan performed with a heating rate of 20°/min up to 1000 °C does not show any noticeable thermal effect. Nevertheless, XRD study of the cooled product (Figure S1, Supporting Information) indicates that the transformation is close to completion. Thus, it is concluded that the phase transformation is sluggish and extended over considerable temperature range. As discussed above, it might proceed by shifting more and more Sb atoms to the Mn layer within an intact crystal with no need for nucleation and growth of the second phase.

The peak positions and lattice parameters in Figure S1b, Supporting Information, match those of the known $P321$ phase. However, only those reflections are sharp that can be indexed with small PbSb_2O_6 -type cell (i.e., having $h^2 + hk + k^2 = 3n$), whereas all other reflections (specific for the $P321$ phase only) are very diffuse. This indicates that the necessary amount of Sb ions has shifted to the Mn layers, but their arrangement still lacks long-range order. The transformation was completed after 1 h calcination at 1100 °C, as evident from Figure S1c and S1d, Supporting Information, where all reflections are sharp.

3.3. Magnetic Properties. The overall behavior of the static magnetic susceptibility $\chi = M/B$ of MnSb_2O_6 obeys a Curie–Weiss law above ~ 50 K (Figure 4). It can be approximated in terms of a modified Curie–Weiss law

$$\chi = \chi_0 + \frac{C}{T - \Theta} \quad (1)$$

with a temperature-independent term χ_0 , the Weiss temperature Θ , and the Curie constant $C = N_A \cdot p_{\text{eff}}^2 \cdot \mu_B^2 / 3k_B$, where N_A is Avogadro's number, p_{eff} is the effective magnetic moment, μ_B is Bohr's magneton, and k_B is Boltzmann's constant. To account for the diamagnetic contribution in MnSb_2O_6 , we estimated $\chi_0 \approx -1.14 \times 10^{-4}$ emu/mol by summing the Pascal's constants.⁵¹

Our analysis yields the Weiss temperature $\Theta = -17(2)$ K, which implies the presence of dominant antiferromagnetic interactions. In addition, we find $p_{\text{eff}} = 5.93(1)$ μ_B per formula unit (FU). Our ESR data, at $T = 300$ K, show a single exchange-narrowed absorption line (see the inset in Figure 4), which is perfectly described by a Lorentzian profile. It is characterized by an effective g factor $g = 1.993 \pm 0.005$, typical of high-spin Mn^{2+} ions ($S = 5/2$) with completely quenched

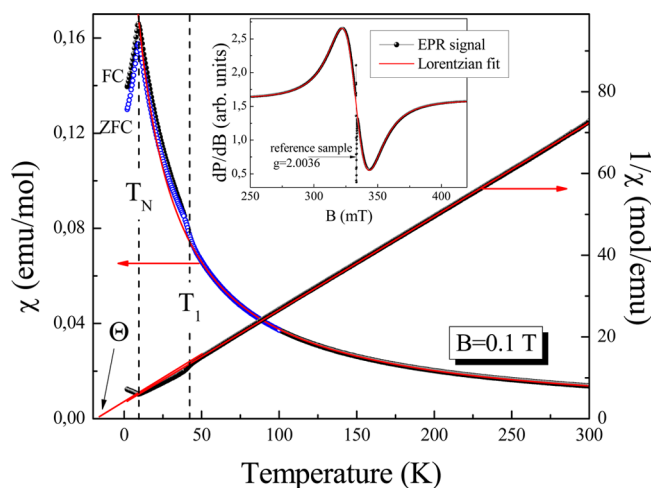


Figure 4. Temperature dependence of the magnetic susceptibility $\chi = M/B$ at $B = 0.1$ T measured after cooling with (FC) and without (ZFC) applied magnetic field. Solid lines represent a Curie–Weiss approximation (see the text). (Inset) ESR spectrum of MnSb_2O_6 recorded with the reference sample BDPA ($g = 2.0036$) at room temperature. Black data points and solid line represent the experimental data and fitting in accordance with a Lorentzian profile, respectively.

orbital moment. The results hence nicely agree with the theoretical estimate of the effective magnetic moment $p^{\text{theor}} = g^2 \mu_B^2 S(S+1) = 5.92 \mu_B/\text{FU}$.

At lower temperatures, there are two anomalies: one at $T_1 = 41.5(5)$ K associated with an increase in the magnetization $\Delta M \approx 1 \times 10^{-3} \mu_B$ per formula unit (FU), and a second one characterized by a sharp maximum in $\chi(T)$ indicating long-range AFM order. Both features in $\chi(T)$ are associated with clear anomalies in the magnetic specific heat, which is proportional to $\partial(\chi T)/\partial T$ and are also visible in the specific heat measurements at zero magnetic field shown in Figure 5. More specifically, the onset of long-range magnetic order is

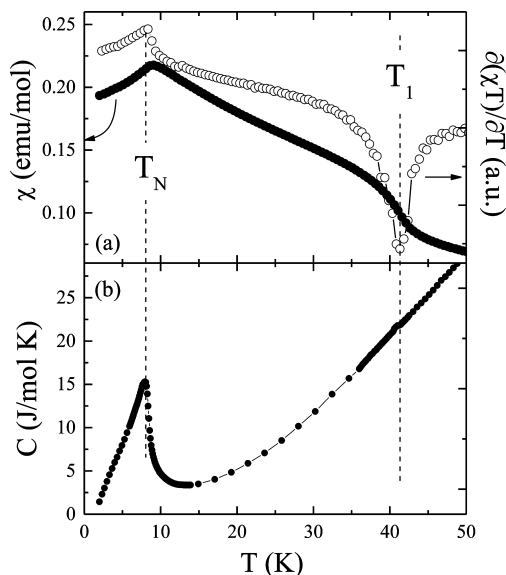


Figure 5. (a) Temperature dependence of the magnetic susceptibility at $B = 0.01$ T, of the magnetic specific heat $\partial(\chi T)/\partial T$, and (b) of the specific heat at $B = 0$ T highlighting two different anomalies at T_N and T_1 .

associated with a λ -like anomaly both in the derivative of the magnetic susceptibility at low magnetic fields and in the specific heat which maximum indicates the Néel temperature $T_N = 8.5(5)$ K. The anomaly size $\Delta C_p \approx 15.3$ J/(mol K) of the λ -like transition at T_N is an upper limit for the actual mean field specific heat jump ΔC_p associated with the continuous onset of long-ranged spin ordering (Figure 5). Still, the mean field result assuming manganese to be in the high-spin Mn^{2+} ($S = 5/2$) state⁵²

$$5R \frac{S(S+1)}{S^2 + (S+1)^2} \approx 19.6 \text{ J/mol}\cdot\text{K} \quad (2)$$

where R is the gas constant, $R = 8.31$ J/(mol K), clearly exceeds the experimentally observed anomaly. Such a reduction in ΔC_p can be indicative of short-range magnetic correlations at temperatures above T_N . The jump ΔM at T_1 and the associated anomaly in $\partial(\chi T)/\partial T$ as well as the corresponding weak anomaly in the specific heat (equivalent to an entropy release of about 0.02 J/mol K) suggest a weak first-order transition. Note a small discrepancy between ZFC and FC curves at $T < T_1$. Correspondingly, the inverse susceptibility shown in Figure 4 deviates from the Curie–Weiss behavior at $T < T_1$. A similar feature has been observed for the related compound NiAs_2O_6 .³⁸

3.4. Density Functional Analysis of Magnetic Structure. While MnSb_2O_6 and MnAs_2O_6 are isostructural electronic analogues, their magnetic properties are not identical, although similar. The magnetic susceptibility of MnAs_2O_6 has a maximum at $T_{\text{max}} \approx 13$ K, the Curie–Weiss temperature amounts to $\Theta = -20.7$ K,³⁸ and neutron diffraction measurements imply long-range magnetic ordering below ~ 12 K associated with an incommensurate superstructure $q = (0.055, 0.389, 0.136)$.³⁸ In comparison, MnSb_2O_6 exhibits $T_{\text{max}} \approx 9$ K, $\Theta = -17$ K, and according to our specific heat and magnetic susceptibility measurements, 3D AFM order appears below $T_N = 8.5$ K. From our macroscopic studies, the specific type of AFM spin ordering cannot be extracted. In order to gain insight into this question, we evaluate the spin exchange interactions of MnSb_2O_6 and compare with those of MnAs_2O_6 .⁴¹

Figure 6a shows a perspective view of the Mn^{2+} ($S = 5/2$) ion arrangement in MnSb_2O_6 , where the blue, pink, and yellow circles represent Mn, Sb, and O atoms, respectively. Figure 6b depicts the associated spin exchange paths between Mn^{2+} ions, where the numbers 1, 2, and 3 indicate the spin exchange paths J_1 , J_2 , and J_3 , respectively. The shortest O...O contacts of J_1 paths are represented by the red arrows in Figure 6a. Here, J_2 is

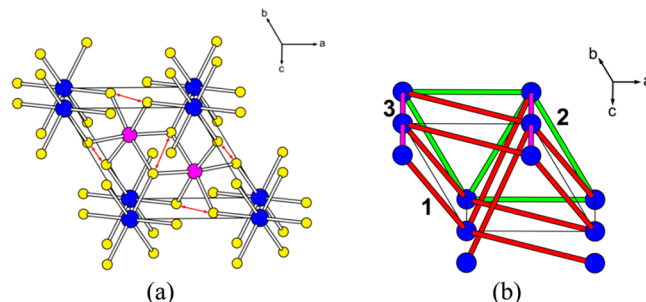


Figure 6. (a) Perspective view of the crystal structure and (b) spin exchange paths in MnSb_2O_6 where the blue, pink, and yellow circles represent Mn, Sb, and O atoms, respectively, and the numbers 1, 2, and 3 indicate the spin exchange paths J_1 , J_2 , and J_3 , respectively.

an intralayer spin exchange path, while J_1 and J_3 are interlayer spin exchange paths.

The energies of these states can be expressed in terms of the spin Hamiltonian

$$\hat{H} = - \sum_{i < j} J_{ij} \hat{S}_i \cdot \hat{S}_j \quad (3)$$

where $J_{ij} = J_1, J_2,$ or J_3 . By applying the energy expression obtained for spin dimers with N unpaired spins per spin sites ($N = 5$ for $M = \text{Mn}$),^{53,54} the total spin exchange energies per (2a, 2b, 2c) supercell, i.e., per 8 FUs, of the different possible states can be written as

$$E = (n_1 J_1 + n_2 J_2 + n_3 J_3)(N^2/4) \quad (4)$$

The coefficients $n_1, n_2,$ and n_3 for the four spin-ordered states FM, AF1, AF2, and AF3 are summarized in Figure 7. The

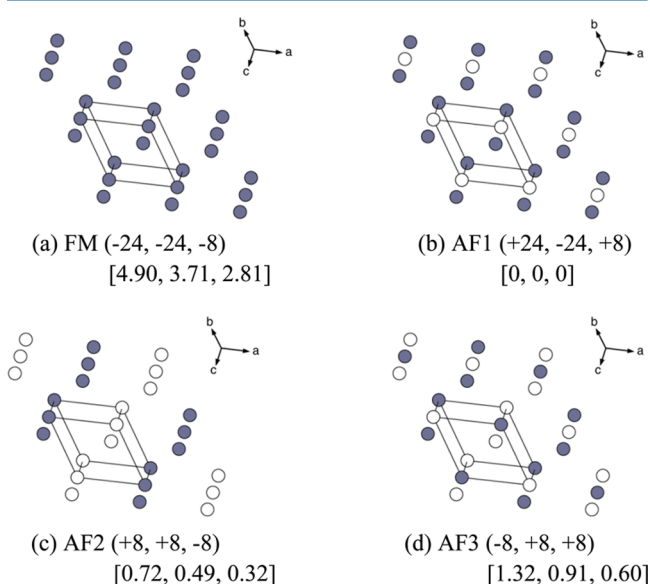


Figure 7. Four ordered spin states (a) FM, (b) AF1, (c) AF2, and (d) AF3 of MnSb_2O_6 employed to extract the values of $J_1, J_2,$ and J_3 , where the gray and white circles represent the up and down spin sites of Mn^{2+} ions. The three numbers in each parentheses (from left to right) refer to the coefficients $n_1, n_2,$ and n_3 of eq 4 for that state, while those in square brackets (from left to right) represent the relative energies (in meV/FU) obtained from DFT+U calculations with $U_{\text{eff}} = 3, 4,$ and 5 eV, respectively.

relative energies of the spin-ordered states can also be calculated on the basis of DFT+U electronic structure calculations. In the case of MnSb_2O_6 at hand, we employed the projected augmented wave (PAW) method encoded in the Vienna ab initio simulation package⁵⁵ and the generalized gradient approximation (GGA) of Perdew, Burke, and Ernzerhof⁵⁶ for the exchange correlations, the plane wave cutoff of 400 eV, and the threshold of self-consistent field (SCF) energy convergence of 10^{-6} eV. The irreducible Brillouin zone was sampled with 54k. To describe the electronic correlation associated with the 3d states of Mn, the DFT plus on-site repulsion U (DFT+U)⁵⁷ calculations were carried out with effective $U_{\text{eff}} = U - J = 3, 4,$ and 5 eV on the Mn atoms. The relative energies of the four ordered spin states determined from our DFT+U calculations are also summarized in Figure 7.

By mapping the energy differences⁵⁴ between the ordered spin states obtained from the DFT+U calculations onto the

corresponding energy differences obtained from the spin Hamiltonian, we obtain the values of $J_1, J_2,$ and J_3 summarized in Table 2.

Table 2. Spin Exchange Parameters (in K) and the Curie–Weiss Temperature Θ (in K) of MnSb_2O_6 Obtained from DFT+U Calculations

	$U = 3$ eV	$U = 4$ eV	$U = 5$ eV
J_1/k_B	−1.28	−0.96	−0.72
J_2/k_B	−0.66	−0.54	−0.44
J_3/k_B	−0.72	−0.57	−0.46
Θ	−38.2	−29.4	−22.9

All three spin exchanges $J_1, J_2,$ and J_3 are AFM. J_1 is the strongest but is not dominant, while J_2 and J_3 are comparable in magnitude. In particular, our results imply that the interlayer spin exchange interactions are stronger than the intralayer ones. If the intralayer exchange J_2 is neglected, the interlayer exchanges J_1 and J_3 form 2D AFM nets. It is also noted that all (J_1, J_2, J_3) triangles are spin frustrated. These results are similar to those found for MnAs_2O_6 .⁴¹ Therefore, one may conclude that MnSb_2O_6 might have an incommensurate magnetic structure, as does MnAs_2O_6 .

4. CONCLUDING REMARKS

By ion-exchange reaction we prepared a new layered trigonal phase of MnSb_2O_6 , which is isostructural with MSb_2O_6 ($M = \text{Cd}, \text{Ca}, \text{Sr}, \text{Pb}, \text{Ba}$) and MAS_2O_6 ($M = \text{Mn}, \text{Co}, \text{Ni}, \text{Pd}$). This new phase is metastable and transformed to the stable one on heating. The transformation is sluggish and proceeds via an intermediate disordered variant of the stable phase. The magnetic susceptibility measurements show that the new MnSb_2O_6 phase exhibits high-spin Mn^{2+} ions and obeys the Curie–Weiss law above ~ 50 K with $\Theta = -17(2)$ K. ESR data show a single absorption line characterized by an effective g factor $g = 1.993 \pm 0.005$, as expected for a high-spin Mn^{2+} ions. The magnetic susceptibility and specific heat measurements show that metastable MnSb_2O_6 undergoes a 3D AFM ordering below $T_N \approx 8.5(5)$ K. In addition, a weak ferromagnetic component appears below $T_1 = 41.5(5)$ K. The spin exchange interactions in MnSb_2O_6 are similar to those of its isostructural electronic analogue MnAs_2O_6 . This predicts an incommensurate magnetic structure for MnSb_2O_6 .

■ ASSOCIATED CONTENT

Supporting Information

Crystallographic information file (CIF) and pdf file containing analytical data, structural models, and additional XRD patterns. This material is available free of charge via the Internet at <http://pubs.acs.org>.

■ AUTHOR INFORMATION

Corresponding Author

*E-mail: vbn@sfedu.ru.

Notes

The authors declare no competing financial interest.

■ ACKNOWLEDGMENTS

V.B.N., E.A.Z., A.Yu.N., and I.L.S. acknowledge support from the Russian Foundation for Basic Research under grant 14-03-01122a. E.A.Z. and R.K. acknowledge support by the Excellence

Initiative of the German Federal Government and States. A.N.V. acknowledges support from the Ministry of Education and Science of the Russian Federation in the framework of Increase Competitiveness Program of NUST MISiS (No. K2-2014-036). The work at NCSU was supported by the computing resources of the NERSC Center and the HPC Center of NCSU. The authors thank anonymous reviewers for useful recommendations and Dr. Yu.V. Popov for microprobe analysis.

REFERENCES

- (1) Misguich, G.; Lhuillier, C. In *Frustrated Spin Systems*; Diep, H. T., Ed.; World Scientific: Singapore, 2004; pp 229–306.
- (2) Richter, J.; Schulenburg, J.; Honecker, A. In *Quantum Magnetism, Lecture Notes in Physics*; Schollwöck, U., Richter, J., Farnell, D. J. J., Bishop, R. F., Eds.; Springer: Berlin, 2004; Vol. 645, pp 85–155.
- (3) Lacroix, C.; Mendels, P.; Mila, F. *Introduction to Frustrated Magnetism: Materials, Experiments, Theory*; Springer: Berlin, 2011.
- (4) Buschow, K. H. J. *Handbook of Magnetic Materials*; Elsevier: Amsterdam, 2001; Vol. 13.
- (5) Greedan, J. E. *J. Mater. Chem.* **2001**, *11*, 37–53.
- (6) Harrison, A. J. *Phys.: Condens. Matter.* **2004**, *16*, S553.
- (7) de Jongh, L. J.; Miedema, A. R. *Adv. Phys.* **1974**, *23*, 1–260.
- (8) Benner, H.; Boucher, J. P. In *Magnetic Properties of Layered Transition Metal Compounds*; Jongh, L. J. de, Ed.; Kluwer Academic Publishers: Dordrecht, Boston, London, 1990; Vol. 9 (Physics and Chemistry of Materials with Low-Dimensional Structures), pp 323–378.
- (9) Diep, H. T.; Giacomini, H. In *Frustrated Spin Systems*; Diep, H. T., Ed.; World Scientific: Singapore, 2004; pp 1–58.
- (10) Vasic, R.; Zhou, H. D.; Jobiliong, E.; Wiebe, C. R.; Brooks, J. S. *Phys. Rev. B* **2007**, *75*, 014436.
- (11) Schulenburg, J.; Honecker, A.; Schnack, J.; Richter, J.; Schmidt, H.-J. *Phys. Rev. Lett.* **2002**, *88*, 167207.
- (12) Honecker, A.; Schulenburg, J.; Richter, J. *J. Phys.: Condens. Matter* **2004**, *16*, S749.
- (13) Richter, J.; Schulenburg, J.; Honecker, A.; Schnack, J.; Schmidt, H.-J. *J. Phys.: Condens. Matter* **2004**, *16*, S779.
- (14) Seabra, L.; Shannon, N. *Phys. Rev. B* **2011**, *83*, 134412.
- (15) Schnack, J.; Schmidt, H.-J.; Richter, J.; Schulenburg, J. *Eur. Phys. J. B* **2001**, *24*, 475–481.
- (16) Richter, J.; Derzhko, O.; Schulenburg, J. *Phys. Rev. Lett.* **2004**, *93*, 107206.
- (17) Derzhko, O.; Richter, J.; Schulenburg, J. *Physica Status Solidi (b)* **2005**, *242*, 3189–3194.
- (18) Derzhko, O.; Richter, J. *Phys. Rev. B* **2005**, *72*, 094437.
- (19) Zhitomirsky, M. E. *Phys. Rev. B* **2003**, *67*, 104421.
- (20) Honecker, A.; Wessel, S. *Phys. B (Amsterdam)* **2006**, 378–380, 1098.
- (21) Derzhko, O.; Richter, J. *Eur. Phys. J. B* **2006**, *52*, 23–36.
- (22) Hemmida, M.; Krug von Nidda, H.-A.; Büttgen, N.; Loidl, A.; Alexander, L. K.; Nath, R.; Mahajan, A. V.; Berger, R. F.; Cava, R. J.; Singh, Y.; Johnston, D. C. *Phys. Rev. B* **2009**, *80*, 054406.
- (23) Drechsler, S.-L.; Volkova, O.; Vasiliev, A. N.; Tristan, N.; Richter, J.; Schmitt, M.; Rosner, H.; Malek, J.; Klingeler, R.; Zvyagin, A. A.; Büchner, B. *Phys. Rev. Lett.* **2007**, *98*, 77202.
- (24) Zvereva, E. A.; Savelieva, O. A.; Titov, Ya.D.; Evstigneeva, M. A.; Nalbandyan, V. B.; Kao, C. N.; Lin, J.-Y.; Presniakov, I. A.; Sobolev, A. V.; Ibragimov, S. A.; Abdel-Hafiez, M.; Krupskaya, Yu.; Jähne, C.; Tan, G.; Klingeler, R.; Büchner, B.; Vasiliev, A. N. *Dalton Trans.* **2013**, *42*, 1550–1566.
- (25) Bramwell, S. T.; Gingras, M. J. P. *Science* **2001**, *294*, 1495–1501.
- (26) (a) Balents, L. *Nature (London)* **2010**, *464*, 199–208.
(b) Drechsler, S.-L.; Richter, J.; Malek, J.; Moskvina, A. S.; Klingeler, R.; Rosner, H. *J. Magn. Magn. Mater.* **2005**, *290–291*, 345–348.
- (27) Kimura, T.; Goto, T.; Shintani, H.; Ishizaka, K.; Arima, T.; Tokura, Y. *Nature (London)* **2003**, *426*, 55–58.
- (28) Cheong, S.-W.; Mostovoy, M. *Nat. Mater.* **2007**, *6*, 13–20.
- (29) Kenzelmann, M.; Harris, A. B.; Jonas, S.; Broholm, C.; Schefer, J.; Kim, S. B.; Zhang, C. L.; Cheong, S.-W.; Vajk, O. P.; Lynn, J. W. *Phys. Rev. Lett.* **2005**, *95*, 087206.
- (30) Arima, T.; Tokunaga, A.; Goto, T.; Kimura, H.; Noda, Y.; Tokura, Y. *Phys. Rev. Lett.* **2006**, *96*, 097202.
- (31) Yamasaki, Y.; Miyasaka, S.; Kaneko, Y.; He, J.-P.; Arima, T.; Tokura, Y. *Phys. Rev. Lett.* **2006**, *96*, 207204.
- (32) Seki, S.; Onose, Y.; Tokura, Y. *Phys. Rev. Lett.* **2008**, *101*, 067204.
- (33) Kimura, K.; Nakamura, H.; Kimura, S.; Hagiwara, M.; Kimura, T. *Phys. Rev. Lett.* **2009**, *103*, 107201.
- (34) Kimura, K.; Nakamura, H.; Ohgushi, K.; Kimura, T. *Phys. Rev. B* **2008**, *78*, 140401(R).
- (35) Vasiliev, A.; Volkova, O.; Presniakov, I.; Baranov, A.; Demazeau, G.; Broto, J. M.; Millot, M.; Leps, N.; Klingeler, R.; Büchner, B.; Stone, M. B.; Zheludev, A. *J. Phys.: Condens. Matter* **2010**, *22*, 016007.
- (36) Terada, N.; Khalyavin, D. D.; Manuel, P.; Tsujimoto, Y.; Knight, K.; Radaelli, P. G.; Suzuki, H. S.; Kitazawa, H. *Phys. Rev. Lett.* **2012**, *109*, 097203.
- (37) Johnson, R. D.; Cao, K.; Chapon, L. C.; Fabrizio, F.; Perks, N.; Manuel, P.; Yang, J. J.; Oh, Y. S.; Cheong, S.-W.; Radaelli, P. G. *Phys. Rev. Lett.* **2013**, *111*, 017202.
- (38) Nakua, A. M.; Greedan, J. E. *J. Solid State Chem.* **1995**, *118*, 402–411.
- (39) Orosel, D.; Jansen, M. Z. *Anorg. Allgem. Chem.* **2006**, *632*, 1131–1133.
- (40) Reehuis, M.; Saha-Dasgupta, T.; Orosel, D.; Nuss, J.; Rahaman, B.; Keimer, B.; Andersen, O. K.; Jansen, M. *Phys. Rev.* **2012**, *B 85*, 115118.
- (41) Koo, H.-J.; Whangbo, M.-H. *Inorg. Chem.* **2014**, *53*, 3812–3817.
- (42) Reimers, J. N.; Greedan, J. E.; Subramanian, M. A. *J. Solid State Chem.* **1989**, *79*, 263–276.
- (43) Hill, R. J. *J. Solid State Chem.* **1987**, *71*, 12–18.
- (44) Castro, A.; Rasines, I.; Sánchez-Martos, M. C.; García-Casado, P. *Powder Diffr.* **1988**, *3*, 219–221.
- (45) DeBoer, B. G.; Young, R. A.; Sakthivel, A. *Acta Crystallogr.* **1994**, *C50*, 476–482.
- (46) Wang, B.; Chen, S. C.; Greenblatt, M. *J. Solid State Chem.* **1994**, *108*, 184–188.
- (47) Nalbandyan, V. B.; Avdeev, M.; Pospelov, A. A. *Solid State Sci.* **2006**, *8*, 1430–1437.
- (48) Larson, A. C.; Von Dreele, R. B. *General Structure Analysis System (GSAS)*; Los Alamos National Laboratory Report LAUR 86-748; Los Alamos National Laboratory: Los Alamos, NM, 2004.
- (49) Toby, B. H. *J. Appl. Crystallogr.* **2001**, *34*, 210–213.
- (50) Shannon, R. D. *Acta Crystallogr. A* **1976**, *32*, 751–767.
- (51) Bain, G. A.; Berry, J. F. *J. Chem. Educ.* **2008**, *85*, 532–536.
- (52) Tari, A. *The specific heat of matter at low temperature*; Imperial College Press: London, 2003.
- (53) (a) Dai, D.; Whangbo, M.-H. *J. Chem. Phys.* **2001**, *114*, 2887–2893. (b) Dai, D.; Whangbo, M.-H. *J. Chem. Phys.* **2003**, *118*, 29–39.
- (54) Xiang, H. J.; Lee, C.; Koo, H.-J.; Gong, X. G.; Whangbo, M.-H. *Dalton Trans.* **2013**, *42*, 823–853 and references cited therein.
- (55) (a) Kresse, G.; Hafner, J. *Phys. Rev. B* **1993**, *47*, 558–561. (b) Kresse, G.; Furthmüller, J. *Comput. Mater. Sci.* **1996**, *6*, 15–50. (c) Kresse, G.; Furthmüller, J. *Phys. Rev. B* **1996**, *54*, 11169–11186.
- (56) Perdew, J. P.; Burke, S.; Ernzerhof, M. *Phys. Rev. Lett.* **1996**, *77*, 3865–3868.
- (57) Dudarev, S. L.; Botton, G. A.; Savrasov, S. Y.; Humphreys, C. J.; Sutton, A. P. *Phys. Rev. B* **1998**, *57*, 1505–1509.